INTERNATIONAL JOURNAL FOR NUMERICAL METHODS IN FLUIDS, VOL. 4, 519–537 (1984)

A METHOD FOR COMPUTING THREE DIMENSIONAL FLOWS USING NON-ORTHOGONAL BOUNDARY-FITTED CO-ORDINATES

C. R. MALISKA* AND G. D. RAITHBY
Department of Mechanical Engineering, University of Waterloo, Waterloo, Ontario, Canada, N2L 3G1

SUMMARY

For three-dimensional fluid flows in complex geometries, it is convenient to make predictions using a non-orthogonal boundary-fitted mesh. The present paper describes an economical method of solving the equations of motion for two and three dimensional problems using such meshes. The locations on the mesh at which the depenent variables are calculated, and the methods used to solve the equations, are key issues in the development of a successful algorithm; these are discussed in the present paper. Results obtained when the proposed method is applied to several problems are also described. The method is intended for flows in which compressibility effects do not dominate.

KEY WORDS Boundary-Fitted Co-ordinates Incompressible Flow 2D and 3D

INTRODUCTION

Many challenging problems face the numerical analyst attempting to predict complex fluid flows. For example, when the fluid Reynolds number is high the convection terms in the equations of motions require special attention in the discretization procedure, an efficient solution method is needed, turbulent transport must be modelled, a strategy for handling irregular boundaries is often required, etc. Finite element developments have, since their beginning, been concerned with the treatment of irregular boundaries while some of the other questions related to fluid flow have, until recently, been largely neglected. The developers of finite volume methods have often focused attention on questions related to the fluid flow and heat transfer while ignoring, again until recently, the problem of treating irregular boundaries. The present paper describes a finite-volume method for calculating a wide range of three-dimensional flows in irregular geometries.

There are three basic methods of treating irregular boundaries. First, a simple (e.g. Cartesian) mesh can be laid out to cover both the solution domain and the boundary; where the boundaries do not coincide with the mesh, interpolation is used in the application of boundary conditions. The problem with this approach is the complexity and inaccuracy that arises in the boundary-condition application. A second alternative is to generate an orthogonal mesh which fits the boundaries. If a suitable orthogonal mesh can be obtained, this approach is numerically attractive; it may, however, be difficult to find such a mesh, especially for three dimensional flows, and to concentrate the grid where greater resolution is needed. The third alternative is to use a non-orthogonal mesh which is also aligned with the boundary. Methods have recently been developed[1–7] to economically generate suitable

* Present address: Mechanical Engineering Dept/UFSC P.O. Box 476, Florianopolis, SC, Brazil

0271–2091/84/060519–19$01.90
© 1984 by John Wiley & Sons, Ltd.
Received 17 November 1982
Revised 22 March 1983

non-orthogonal meshes for complex geometries, including the option of increasing grid resolution where detail is required. The disadvantage of this approach is that the computer code required to solve the equations of motion becomes more complex. Despite this disadvantage such methods may be nearly optimal provided good discretization and solution methods can be developed.

The grids of particular interest here are those which form curvilinear quadrilaterals in two dimensions, and curvilinear hexahedra in three dimensions. Such grids can often be generated manually or by using simple geometric relations; the grid covering a subchannel region of a fuel bundle, proposed by Ramachandra and Spalding,[8] and the sigma co-ordinates of Phillips,[9] fall into these categories. For more complex regions, including multiply-connected domains, the grid generation methods of Chu,[2] Winslow,[1] and Thompson, Thames, and Mastin[10] can be used.

The goal of the present study was to develop and test a finite volume method for solving elliptic two dimensional (2D) and three dimensional (3D) fluid flow problems using non-orthogonal grids. The treatment of 3D parabolic flows was the primary target, but the method should be extendable to 3D elliptic flows.

Several recent studies[11–18] have had similar goals, but the present method introduces some desirable novel features, and its predictive capabilities have been perhaps more exhaustively tested for truly elliptic flows. A detailed review of the state-of-the-art has been provided by Maliska.[19]

This paper does not contribute to procedures for generating non-orthogonal boundary-fitted meshes; the methods of Thompson, Thames, and Mastin[3,10] are extensively used.

GENERATION OF CO-ORDINATE SYSTEM

If the flow and heat transfer inside an irregular duct, such as shown in Figure 1(a), is required, the first step is to transform the flow area into the parallelepiped shown in Figure 1(b). With the restriction that there is a simple stretching in the z-direction, the transformation takes the form

$$\xi = \xi(x, y, z); \qquad \eta = \eta(x, y, z); \qquad \Gamma = z \tag{1}$$

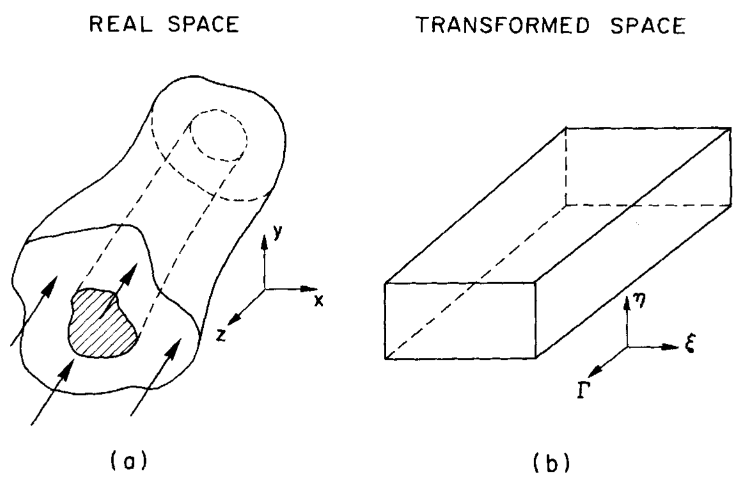

Figure 1. Duct of arbitrary cross-section in the real plane (a) and the transformed plane (b)

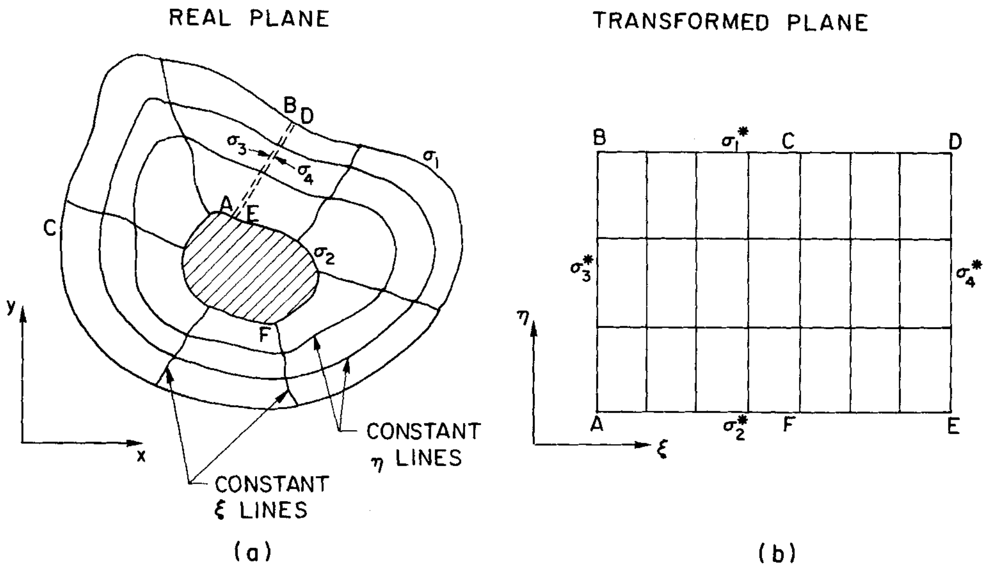

Figure 2. Co-ordinate lines for a given cross-section in the real (a) and transformed (b) planes

The above transformation applies to any straight duct, but may also be applied when the duct centreline curvature is mild. Cross-sections of the duct in the real (x, y) plane and transformed (ξ, η) plane is shown in Figure 2. With an arbitrary grid spacing in the transformed plane (e.g. $\Delta\eta = \Delta\xi = 1$), the grid in the ξ, η plane can be constructed and the particular transformation used will determine where these lines fall in the corresponding cross-section in the x, y plane.

For the type of transformation in equation (1), the grid over the entire 3D domain of interest can be generated from a fully three dimensional transformation, or the locations of the computational planes in the z-direction can be specified and a two-dimensional transformation can be generated for each z-plane. The present study adopted the latter strategy. Thompson, Thames, and Mastin[10] provide the mathematical motivation for choosing the following elliptic equations to generate this transformation

$$\xi_{xx} + \xi_{yy} = P(\xi, \eta) \tag{2}$$

$$\eta_{xx} + \eta_{yy} = Q(\xi, \eta) \tag{3}$$

The boundary conditions for equation (3) are the specified η values on the σ_1 and σ_2 surfaces in Figure 2(a); for these boundary conditions and from the form of equation (3), it can be seen that η plays the same role as temperature in a heat conduction problem with a source-term distribution, Q. The desired transformation locates the position of the η-'isotherms' in the real plane that have already been drawn in the transformed plane. Except for the boundary condition specification, ξ in equation (2) can be similarly interpreted.

Because the application of boundary conditions to equations (2) and (3) is complicated by the irregular geometry, the independent and dependent variables are interchanged.[10] This results in somewhat more complex differential equations for $x(\xi, \eta)$ and $y(\xi, \eta)$, but the boundary conditions are easily applied and the solution is straightforward. The distributions of P and Q are chosen to concentrate the grid lines in the desired regions. The reader is referred to References 3 and 10 for more details related to the transformation.

TRANSFORMATION OF THE EQUATIONS OF MOTION

The differential equations of motion are required as the starting point for the solution in the transformed space where ξ, η and Γ are the independent variables. One can write these equations directly, using the velocity components normal to the $\xi=$ constant, $\eta=$ constant and $\Gamma=$ constant surfaces (contravariant components) respectively as dependent variables, as outlined by Warsi, Devarayalu, and Thompson,[13] but the equations are complex. Another alternative[16,18] is to write the equations of motion in the physical plane in any convenient co-ordinate system (e.g. Cartesian, circular cylinder) and transform these to the general non-orthogonal system while maintaining the same dependent variables. This study adopted the latter strategy because it gives rise to relatively simple equations. The equations of motion in Cartesian co-ordinates were taken as the starting point in the present method.

For a variable ϕ, where ϕ may be unity (mass conservation), u, v and w (momentum conservation), T (energy conservation), etc., the conservative form of the ϕ-conservation equation in a Cartesian system is

$$\frac{\partial}{\partial t}(\rho\phi)+\frac{\partial}{\partial x}(\rho u\phi)+\frac{\partial}{\partial y}(\rho v\phi)+\frac{\partial}{\partial z}(\rho w\phi)+P^{\phi}=\frac{\partial}{\partial x}\left(\Gamma^{\phi}\frac{\partial\phi}{\partial x}\right)+\frac{\partial}{\partial y}\left(\Gamma^{\phi}\frac{\partial\phi}{\partial y}\right)+\frac{\partial}{\partial z}\left(\Gamma^{\phi}\frac{\partial\phi}{\partial z}\right)+S^{\phi} \tag{4}$$

In this equation Γ^{ϕ} is the coefficient of ϕ diffusion, P^{ϕ} is the pressure gradient term (where appropriate), and S^{ϕ} is an accumulation of source terms not explicitly represented by the remaining terms in the equation.

For many duct flow problems, the strong component of velocity in the z-direction in Figure 1 makes it reasonable to introduce a parabolic approximation.[20] This permits the solution to be marched forward plane-by-plane, with a 2D elliptic problem being solved on each plane. In this case the pressure is split into two components as follows:

$$P(x, y, z)=\tilde{P}(x, y; z)+\bar{P}(z) \tag{5}$$

and the second to last term in equation (4) is dropped.

Equation (4), without the z-diffusion term, is now transformed to the ξ, η, Γ co-ordinate system. The transformation described by Peyret and Viviand[21] is used because the transformed equations that result are in the desired conservative form:

$$\frac{\partial\rho\phi}{\partial t}+\frac{\partial}{\partial\xi}(\rho U\phi)+\frac{\partial}{\partial\eta}(\rho V\phi)+\frac{\partial}{\partial\Gamma}(\rho W\phi)+\hat{P}^{\phi}=\frac{\partial}{\partial\xi}\left(C_1\frac{\partial\phi}{\partial\xi}+C_2\frac{\partial\phi}{\partial\eta}\right)+\frac{\partial}{\partial\eta}\left(C_3\frac{\partial\phi}{\partial\eta}+C_4\frac{\partial\phi}{\partial\xi}\right)+\hat{S}^{\phi} \tag{6}$$

The U, V, and W in this equation are the contravariant velocity components written without metric normalization, so that (for example) $\rho U\phi$ represents the convection of ϕ per unit area across a surface of constant ξ. The relationships between the Cartesian and contravariant velocity components are:

$$U=y_{\eta}u-x_{\eta}v+(y_{\Gamma}x_{\eta}-x_{\Gamma}y_{\eta})w \tag{7a}$$

$$V=x_{\xi}v-y_{\xi}u+(x_{\Gamma}y_{\xi}-y_{\Gamma}x_{\xi})w \tag{7b}$$

$$W=\frac{w}{J} \tag{7c}$$

where $J^{-1}=(x_{\xi}y_{\eta}-x_{\eta}y_{\xi})$ is the Jacobian of the transformation between a given physical plane and the corresponding transformed plane, and $\Gamma=z$ [i.e. equation (1)] has been used. The

Table I. Source terms $\hat{P}^{\phi}$ and $\hat{S}^{\phi}$ for ϕ of u, v, and w

$$\hat{P}^{u}=\frac{\partial P}{\partial \xi}\frac{\partial y}{\partial \eta}-\frac{\partial P}{\partial \eta}\frac{\partial y}{\partial \xi}$$

$$\hat{P}^{v}=\frac{\partial P}{\partial \eta}\frac{\partial x}{\partial \xi}-\frac{\partial P}{\partial \xi}\frac{\partial x}{\partial \eta}$$

$$\hat{P}^{w}=\frac{1}{J}\frac{\mathrm{d}\bar{P}}{\mathrm{d}\Gamma}$$

$$\hat{S}^{u}=J(y_\eta\mu_\xi-y_\xi\mu_\eta)(y_\eta u_\xi-y_\xi u_\eta)+J(y_\eta v_\xi-y_\xi v_\eta)(x_\xi\mu_\eta-x_\eta\mu_\xi)$$
$$+J(y_\eta w_\xi-y_\xi w_\eta)\left[(y_\Gamma x_\eta-x_\Gamma y_\eta)\mu_\xi+(x_\Gamma y_\xi-y_\Gamma x_\xi)\mu_\eta+\frac{1}{J}\mu_\Gamma\right]$$

$$\hat{S}^{v}=J(x_\xi u_\eta-x_\eta u_\xi)(y_\eta\mu_\xi-y_\xi\mu_\eta)+J(x_\xi v_\eta-x_\eta v_\xi)(x_\xi\mu_\eta-x_\eta\mu_\xi)$$
$$+J(x_\xi w_\eta-x_\eta w_\xi)\left[(y_\Gamma x_\eta-x_\Gamma y_\eta)\mu_\xi+(x_\Gamma y_\xi-y_\Gamma x_\xi)\mu_\eta+\frac{1}{J}\mu_\Gamma\right]$$

$$\hat{S}^{w}=J(y_\eta\mu_\xi-y_\xi\mu_\eta)\left[(y_\Gamma x_\eta-x_\Gamma y_\eta)u_\xi+(x_\Gamma y_\xi-y_\Gamma x_\xi)u_\eta+\frac{1}{J}u_\Gamma\right]$$
$$+J(x_\xi\mu_\eta-x_\eta\mu_\xi)\left[(y_\Gamma x_\eta-x_\Gamma y_\eta)v_\xi+(x_\Gamma y_\xi-y_\Gamma x_\xi)v_\eta+\frac{1}{J}v_\Gamma\right]$$
$$+J\left(\left[(y_\Gamma x_\eta-x_\Gamma y_\eta)w_\xi+(x_\Gamma y_\xi-y_\Gamma x_\xi)w_\eta+\frac{1}{J}w_\Gamma\right]\right.$$
$$\left.\times\left[(y_\Gamma x_\eta-x_\Gamma y_\eta)\mu_\xi+(x_\Gamma y_\xi-y_\Gamma x_\xi)\mu_\eta+\frac{1}{J}\mu_\Gamma\right]\right)$$

coefficients are given by

$$C_1=\Gamma^{\phi}J\alpha \tag{8a}$$

$$C_2=C_4=-\Gamma^{\phi}J\beta \tag{8b}$$

$$C_3=\Gamma^{\phi}J\gamma \tag{8c}$$

where $\alpha=x_\eta^2+y_\eta^2$, $\beta=x_\xi x_\eta+y_\xi y_\eta$, and $\gamma=x_\xi^2+y_\xi^2$. The $\hat{P}^{\phi}$ and $\hat{S}^{\phi}$ terms are defined in Table I for each dependent variable. The $\hat{S}$ terms vanish when viscosity, μ, is constant.

DISCRETE EQUATIONS

Grid layout for the dependent variables

The importance of choosing an appropriate grid layout for the dependent variables can hardly be overemphasized because of the consequences of this choice on the form (and thus on the ease of solution) of the discrete equations, and the accuracy of the solution obtained. The motivation for choosing the grid used in this study is, therefore, presented in some detail.

Several important points can be illustrated for the case when ξ, η forms a Cartesian mesh in the physical plane with $u=U$ and $v=V$. The non-orthogonal method should be able to treat problems in which these conditions prevail over a subsection of, or all of, the solution domain. After a discussion of this special case, attention is turned to some of the other considerations which arise when these conditions are violated. As an introduction, it is appropriate to emphasize that the mass conservation equation is, in the incompressible

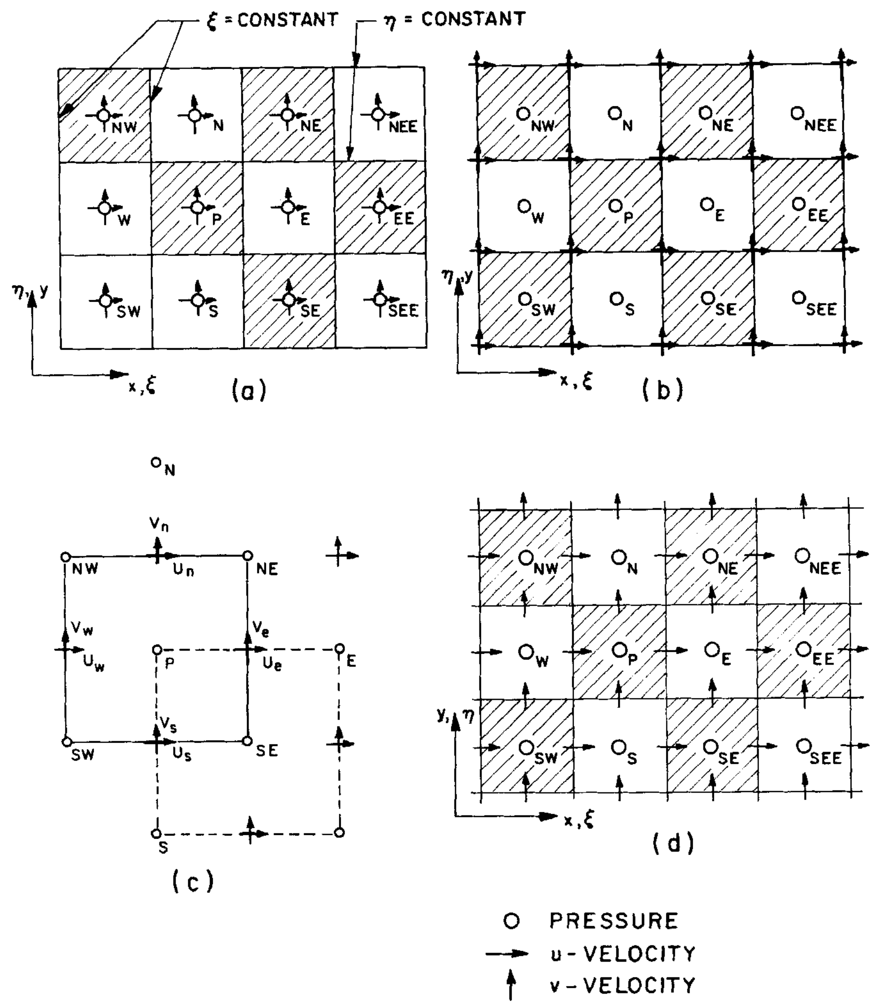

Figure 3. Various possible grid configurations for which $u = U$ and $v = V$

formulation, primarily an equation for pressure rather than density.[22] That is, the validity of any assumed pressure distribution is checked by determining whether or not the velocities that are obtained from the momentum equations, using this pressure, conserve mass.

Most non-orthogoonal methods[10–17] locate pressure and velocity at the same grid locations, as shown for two dimensions in Figure 3(a). For the special case under consideration, that is $u = U$ and $v = V$, the momentum equation for u_P uses an approximation of the pressure gradient in the ξ-direction that involves only P_E and P_W. Similarly the equation for u_E involves only P_{EE} and P_P. A chequerboard pattern results in which the pressures at the centre of the 'shaded' areas drive the velocities in the 'non-shaded' areas whereas the pressures in the non-shaded areas drive only the velocities in the shaded areas. These two pressure fields are only loosely tied together through boundary conditions. The disadvantages of such a system include solution difficulties and apparently erratic (unless one only plots the velocities from the non-shaded areas and pressures from the shaded areas) results. A more detailed discussion is provided by Patankar.[23]

An alternative grid layout used by Vanka, Chen, and Sha[18] is shown for the special case under consideration in Figure 3(b). In this grid pressures are located at the centres of the control volumes and the velocities are located at the corners. To evaluate the pressure gradient which drives the u-velocity at the upper right corner of the control volume centred at P, the average of P_N with P_P is subtracted from the average of P_{NE} with P_E. Mass conservation for the control volume centered at P is checked using a velocity for each face obtained through an average of the velocities at the corners. These two averaging processes lead to the result that mass conservation for the P-control volume is satisfied if the corner pressures (P_{NE}, P_{SE}, P_{SW} and P_{NW}) and P_P are correct, independent of the pressures P_E, P_W, P_N, and P_S. Similarly, mass conservation for the control volume centred at E provides a constraint only for pressures P_N, P_{NEE}, P_{SEE}, P_S, and P_E. A chequerboard pattern again emerges in which pressures at the centres of the shaded areas are very nearly decoupled from those at the centres of the unshaded areas. The solution difficulties that arise when such behaviour is permitted are described by Vanka, Chen, and Sha.[18]

If the velocities in the shaded areas and pressures on the non-shaded areas in Figure 3(a) are eliminated, the grid layout shown in Figure 3(c) results. The pressure and velocities are now suitably staggered, but there is still weak coupling between the pressures at P, E, N, W, S,... and those at NE, SE, SW, NW,.... Conservation of mass for the control volume centred at P depends only on the velocities normal to its faces (U_e, U_w, V_s and V_n) which are in turn, for this special case, depend through momentum only on P_E, P_W, P_N, P_S, and P_P. If these pressures are correct, mass conservation for the control volume centred at P will be satisfied even though the pressure P_{NE}, P_{SE}, P_{SW}, and P_{NW} are completely wrong. The latter pressures are checked by mass conservation for the control volume centred at SE in Figure 3(c). Again, two nearly independent pressure distributions are present that are only weakly coupled through boundary conditions.

If one of the two uncoupled pressure fields in Figure 3(c) is eliminated, together with the velocities driven by these pressures, the grid layout shown in Figure 3(d) results. This is the classical staggered mesh of Harlow and Welch.[24] It will be seen that all the problems related to the other meshes have been removed.

We now depart from the special case just considered and suppose instead that, although the ξ, η grid is still Cartesian (locally or globally) in the physical plane, the Cartesian velocities (u, v) are not aligned with the contravariant velocities (U, V), as shown in Figure 4.

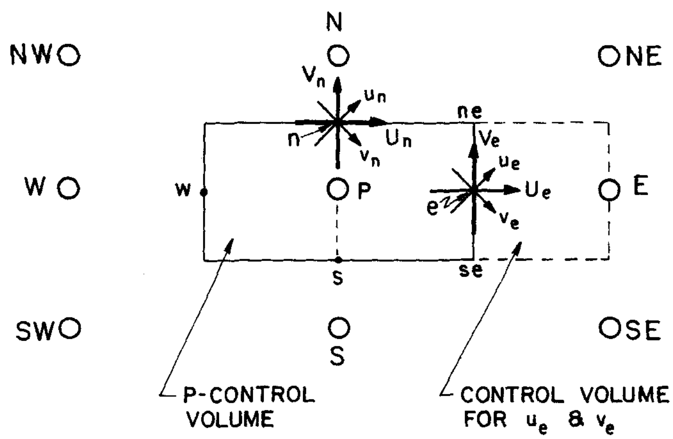

Figure 4. A grid for which Cartesian and contravariant velocities are not aligned

In this case the u, v velocities at the centre of each control-volume face are driven through the momentum equations by the pressures at the six surrounding pressure points. If the pressure distribution used is correct, the components of u and v which give the contravariant velocities normal to the faces (such as U_e, U_w, V_s, and V_n) must satisfy mass conservation. However, the components of u and v which give the contravariant velocities that lie parallel to the faces of the control volume shown (V_e, U_s, V_w, and U_n), are unconstrained by mass conservation. This freedom often results in oscillations or divergence when a solution is attempted or, if a solution can be found, the contravariant velocities that are not subject to mass conservation often appear to be erratic when compared to those that do satisfy a mass constraint. To force both the contravariant velocities to conserve mass, extra pressure points would have to be inserted at the corners of the control volume in Figure 4. But this leads to the grid in Figure 3c which has already been rejected.

An answer to this apparent dilemma is to use the computed Cartesian velocities (u, v) only to calculate the contravariant velocity components that enter the mass conservation constraint (i.e. U_e, V_n, etc. in Figure 4). If the other components, such as V_e or U_n, are required for any reason, these should *not* be obtained from the Cartesian velocities u and v, but rather by interpolation using the U and V values that are constrained by mass conservation. This strategy has been found to eliminate solution difficulties and to yield convergence rates that are about the same as those for the corresponding formulation that is restricted to Cartesian grids.

The same strategy can be used for a 3D non-orthogonal mesh, such as shown in Figure 5(a). The application of these ideas to the solution procedure used will be detailed in a later section.

Discrete equations

The solution domain is divided into volumes such as shown in Figure 5, and in cross-section in Figure 4, and for each such volume the discrete values of the w-velocity and pressure at the centre are sought (i.e. w_P and P_P), together with the u- and v-velocities at the centre of each face (i.e. u_e, v_e, u_n, v_n, u_w, v_w, u_s, and v_s). To obtain the equation for w_P, the

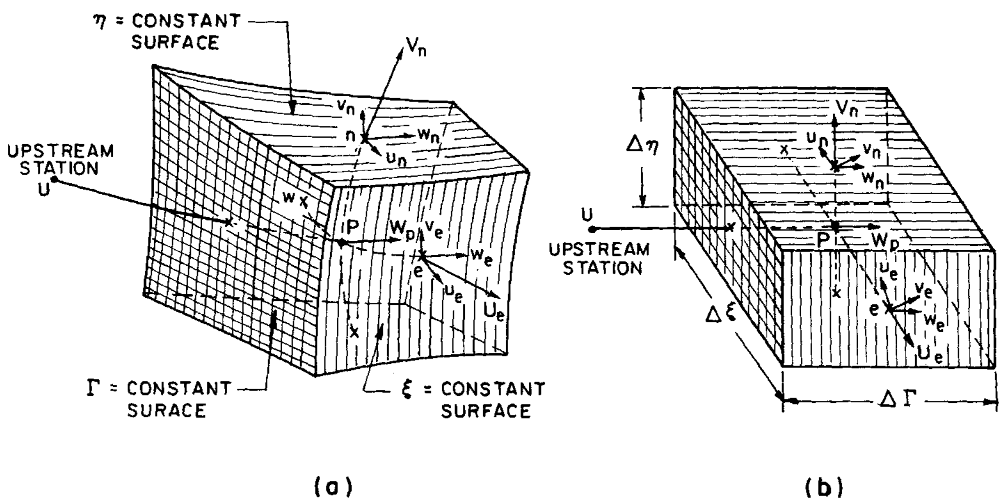

Figure 5. Typical control volumes in the real and transformed planes

w-momentum equation is integrated over the volume, ΔV, and approximations are introduced[22,25] to reduce the integral equation to the algebraic equation

$$A_P w_P^{n+1} = A_E w_E^{n+1} + A_W w_W^{n+1} + A_N w_N^{n+1} + A_S w_S^{n+1} + A_U w_{P,U} + \frac{A_P}{1+E} w_P - \frac{\Delta \bar{P}}{\Delta \Gamma} \frac{\Delta V}{J_P} + L[\widehat{ST}^w] \Delta V \tag{9a}$$

The $n+1$ superscript denotes the unknowns in the equation, whereas all other terms and coefficients are based on best-available estimates. The operator L [ ] represents the finite difference approximation of the quantity in brackets. The coefficients are

$$A_E = -(\rho U)_e \Delta\eta\, \Delta\Gamma(\tfrac{1}{2} - \bar{\alpha}_e) + \bar{\beta}_e C_{1e} \Delta\eta\, \Delta\Gamma/\Delta\xi \tag{9b}$$

$$A_W = (\rho U)_w \Delta\eta\, \Delta\Gamma(\tfrac{1}{2} + \bar{\alpha}_w) + \bar{\beta}_w C_{1w} \Delta\eta\, \Delta\Gamma/\Delta\xi \tag{9c}$$

$$A_P^* = (A_E + A_W + A_N + A_S + A_U); \qquad A_P = A_P^*(1+E)/E \tag{9d}$$

$$\widehat{ST}^w = \hat{S}^w + \frac{\partial}{\partial\xi}\left(C_2 \frac{\partial w}{\partial\eta}\right) + \frac{\partial}{\partial\eta}\left(C_4 \frac{\partial w}{\partial\xi}\right) \tag{9e}$$

where the lower case subscripts denote face locations (Figure 4) and $\bar{\alpha}$ and $\bar{\beta}$ are weights on the convection and diffusion terms[25] which maintain positive coefficients. Equation (9a) can be written more compactly[23] as

$$A_P w_P = \sum A_{nb} w_{nb} + B_P^w - \frac{\Delta \bar{P}}{\Delta \Gamma} \frac{\Delta V}{J_P} \tag{10}$$

where nb represents the 'neighbours' of the dependent variable on the left side of the equation.

The equations for u_e and v_e are obtained by integration of the u- and v-momentum equations over the control volume with dashed boundaries shown in Figure 4. These have the form

$$A_e u_e = \sum A_{nb} u_{nb} + B_e^u - \Delta V \left\{ \frac{P_E - P_P}{\Delta\xi} (y_\eta)_e - \frac{P_N + P_{NE} - P_S - P_{SE}}{4\,\Delta\eta} (y_\xi)_e \right\} \tag{11}$$

$$A_e v_e = \sum A_{nb} v_{nb} + B_e^v - \Delta V \left\{ \frac{P_N + P_{NE} - P_S - P_{SE}}{4\,\Delta\eta} (x_\xi)_e - \frac{P_E - P_P}{\Delta\xi} (x_\eta)_e \right\} \tag{12}$$

where the A_e and A_{nb} are the same in both equations. Similar equations are written for u_n, v_n, u_w, v_w, etc.

The pressure equation will be derived from the following mass-conservation equation for the volume in Figures 4 and 5

$$[(\rho U)_e - (\rho U)_w] \Delta\eta\, \Delta\Gamma + [(\rho V)_n - (\rho V)_s] \Delta\xi\, \Delta\Gamma + [(\rho W)_P - (\rho W)_U] \Delta\xi\, \Delta\eta = 0 \tag{13}$$

The contravariant velocities at each face (e.g. U_e) are related through equation (7a) to the Cartesian velocities (e.g. u_e, v_e, and w_e) at the face.

Solution procedure

In a 3D-parabolic solution, all the velocities and pressures are iterated to convergence in a given Γ-plane before commencing with the solution on the next downstream Γ-plane. Each iteration within a given Γ-plane, which results in updated values of the dependent variables in that plane, is defined here as an 'outer' iteration. Each outer iteration involves an update of the coefficients in the algebraic equations being solved, using best available estimates of the required variables.

In the proposed solution procedure, the first steps in an outer iteration involve the update of the coefficients in equation (10), and the solution for w_p. The solution method used[22] evaluates the presssure gradient $\Delta\bar{P}/\Delta\Gamma$ so that the w-values obtained both satisfy the momentum equation and yield the correct total mass flow. Equation (7c) is used to convert w_p to W_p.

The next step is to solve for the velocities and pressures in a transverse plane. Two solution methods were used,[19] but the discussion here is restricted to the method which was based on the well-known SIMPLER procedure of Patankar.[23] According to this approach, the u- and v-momentum equations are first solved using the best available pressure, P^*. The velocities obtained do not conserve mass, so these are denoted by u^* and v^*. The corresponding values U^* and V^* are obtained by substituting these, together with the w from step 1, into equations (7a) and (7b). These velocities must be then corrected by $U-U^*$ and $V-V^*$, respectively to obtain U and V velocities which do conserve mass. These changes are related through equation (7) to the corresponding required changes in the u and v velocities as follows:

$$U-U^*=y_\eta(u-u^*)-x_\eta(v-v^*) \tag{14a}$$

$$V-V^*=x_\xi(v-v^*)-y_\xi(u-u^*) \tag{14b}$$

Following the SIMPLER procedure, estimates of the change in u and v that result from the change in P of $P'=P-P^*$ are, from equations (11) and (12):

$$u_e-u_e^*=-\frac{\Delta V}{A_e}\left\{\frac{P'_E-P'_P}{\Delta\xi}(y_\eta)_e-\frac{P'_N+P'_{NE}-P'_S-P'_{SE}}{4\Delta\eta}(y_\xi)_e\right\} \tag{15a}$$

$$v_e-v_e^*=-\frac{\Delta V}{A_e}\left\{\frac{P'_N+P'_{NE}-P'_S-P'_{SE}}{4\,\Delta\eta}(x_\xi)_e-\frac{P'_E-P'_P}{\Delta\xi}(x_\eta)_e\right\} \tag{15b}$$

Similar expressions can be written for $u_n-u_n^*$, $v_n-v_n^*$, $u_w-u_w^*$, $v_w-v_w^*$, $u_s-u_s^*$ and $v_s-v_s^*$. These are substituted into equation (14) to obtain equations for U and V in terms of U^*, V^*, and P'. The following equation is then derived by substituting the values of U_e, U_w, V_n, and V_s so obtained into the continuity constraint, equation (13):

$$A_PP'_P=A_EP'_E+A_WP'_W+A_NP'_N+A_SP'_S+A_{NE}P'_{NE}+A_{NW}P'_{NW}+A_{SE}P'_{SE}+A_{SW}P'_{SW}+B \tag{16}$$

where the coefficients in this equation are given by

$$A_E=\frac{\Delta\Gamma}{A_e}\alpha_e+\frac{\Delta\Gamma}{4A_s}\beta_s-\frac{\Delta\Gamma}{4A_n}\beta_n;\qquad A_W=\frac{\Delta\Gamma}{A_w}\alpha_w-\frac{\Delta\Gamma}{4A_s}\beta_s+\frac{\Delta\Gamma}{4A_n}\beta_n \tag{17}$$

$$A_N=\frac{\Delta\Gamma}{A_n}\gamma_n+\frac{\Delta\Gamma}{4A_w}\beta_w-\frac{\Delta\Gamma}{4A_e}\beta_e;\qquad A_S=\frac{\Delta\Gamma}{A_s}\gamma_s-\frac{\Delta\Gamma}{4A_w}\beta_w+\frac{\Delta\Gamma}{4A_e}\beta_e \tag{18}$$

$$A_{NE}=-\frac{\Delta\Gamma}{4A_e}\beta_e-\frac{\Delta\Gamma}{4A_n}\beta_n;\qquad A_{SE}=\frac{\Delta\Gamma}{4A_e}\beta_e+\frac{\Delta\Gamma}{4A_s}\beta_s \tag{19}$$

$$A_{NW}=\frac{\Delta\Gamma}{4A_w}\beta_w+\frac{\Delta\Gamma}{4A_n}\beta_n;\qquad A_{SW}=-\frac{\Delta\Gamma}{4A_w}\beta_w-\frac{\Delta\Gamma}{4A_s}\beta_s \tag{20}$$

$$A_p=A_E+A_N+A_W+A_S;\qquad A_{NE}+A_{NW}+A_{SE}+A_{SW}=0 \tag{21}$$

B is the mass source of the U^*, V^*, W field divided by $\rho\Delta V$; for simplicity in writing equations (17)–(20). $\Delta\xi$ and $\Delta\eta$ were taken as unity.

In these coefficients α, β, and γ are the components of the metric tensor, defined in the text following equation (8), evaluated at the points in Figure 4 denoted by their subscripts. A_e is the central coefficient in the u_e- or v_e-equation (equations (11) and 12); similarly A_n, A_w, ... are the central coefficients in the equations for u_n or v_n, u_w or v_w, ... The negative coefficients that appear in equations (17)–(20) are undesirable because of the potential for higher solution cost when iterative solvers are used. In practice, however, the magnitudes of these terms are sufficiently small that convergence does not seem to be significantly affected.

Once P' is known the contravariant velocities which enter into the mass balance (U_e, U_w, V_s, V_n, etc.) can be found from equations (15) and (14). The other contravariant velocities, such as V_e, U_n, are interpolated from their mass-conserving counterparts, as described in the section describing the grid layout. To then obtain the corrected Cartesian velocities u and v, equation (7) is rearranged to obtain u and v explicitly in terms of U and V, and new U and V values are substituted. The stability of the scheme and accuracy of the results are both tied to finding u and v in this manner, as already discussed.

The next step is to update the pressure. Following the SIMPLER[20] (or PUP[26]) procedure the momentum coefficients are updated and an equation, identical to equation (16) except for the source term, is solved for P.

This completes one outer iteration. The convergence is checked, and if the convergence criterion is not satisfied further outer iterations are performed until convergence is achieved.

The sequence of steps is therefore as follows:

1. The coefficients for all equations are calculated using best available velocities.
2. The w-momentum equations (such as equation (10)) are solved, and the axial pressure gradient $\Delta\bar{P}/\Delta\Gamma$ determined.
3. With the best available pressure, the cross-flow momentum equations (such as equations (11) and (12)) are solved for u^* and v^*. The corresponding contravariant velocities U^*, V^* are found from equation (7).
4. The P'-equation is then solved, and the solution used to correct U^* and V^* to U and V through equations (14) and (15). The corrected velocities conserve mass. The other contravariant velocities that lie parallel to the control volume face, are then found by interpolation using the newly computed U, V velocities.
5. The corrected values of u and v are then found from equation (7).
6. The pressure in the cross-flow plane is obtained using the SIMPLER method.[23] This requires the solution of equation (16), with P' replaced by P.
7. If convergence has not been achieved, return to step 1 and repeat the steps.

Because of the alternate use of the Cartesian and contravariant velocities, the above procedure is somewhat more complex than the corresponding SIMPLER procedure applied to an orthogonal formulation. In addition twice as many momentum equations must be solved (i.e. two velocities per control volume face rather than one) and the extra velocities stored. These detractions are not as great as they might at first appear. Only a few iterations are required to solve the momentum equations to sufficient accuracy so that the incremental cost of solving the extra equation is small. The coefficients are the same for both velocities at each face so that extra storage is needed only for the added velocity, its source term, and the contravariant velocities. The advantage of the method lies in the tight coupling between the velocity and pressure fields, which leads to rapid convergence of the equation set.

APPLICATIONS

It is a common practice to test three-dimensional parabolic codes by solving for the developing flow in ducts whose cross-sections are invariant with axial distance, and by checking the predicted pressure gradient and the flow in the axial direction against previous numerical, experimental or analytical results. The secondary velocities (i.e. the velocities normal to the principal flow direction) in such flows are normally small, and it has been the authors' experience that setting these velocities to zero, so that only the axial momentum equation is satisfied, has no appreciable effect on the comparisons. Solving such problems, therefore, does not provide adequate verification.

In the present study the ability of the method to treat truly elliptic effects in the cross-flow was first tested by setting the axial velocity to zero and by solving several two dimensional problems in the cross-flow plane. Then the three-dimensional parabolic flow in the entrance region of a circular duct was solved to test the solution of the axial-flow momentum equation. Finally, the flow in a complex converging-diverging duct was solved to show the flexibility and generality of the numerical model.

Driven flow in a square cavity

The first test is concerned with the recirculating flow in a square cavity. Figure 6 shows the geometric parameters and the boundary conditions for the problem. The tests were performed for $Re = 100$ and 400 so that flows with both predominant diffusion and convection were analysed. For both cases the problem was solved using a 28×28 uniform Cartesian grid, and the 28×28 non-orthogonal grid shown in Figure 6(b); the numerical solutions obtained using these grids were then compared.

In generating the non-orthogonal mesh the region with high non-orthogonality was chosen to lie close to the moving wall and close to the region of high pressure (i.e. near the lower left corner). This attempts to impose on the code the most severe test conditions. Coordinate attraction was used whereby the η-lines were forced to concentrate near to the moving wall, and the ξ-lines near the left wall.

For $Re = 100$, the velocities and pressures obtained using the orthogonal and non-orthogonal grids were in excellent agreement; in addition, these results agreed well with the predictions of Burggraf.[27] For $Re = 400$ the two grids again yielded nearly identical predictions of pressure, and the velocities were in quite close agreement, as seen in Figure 7. This

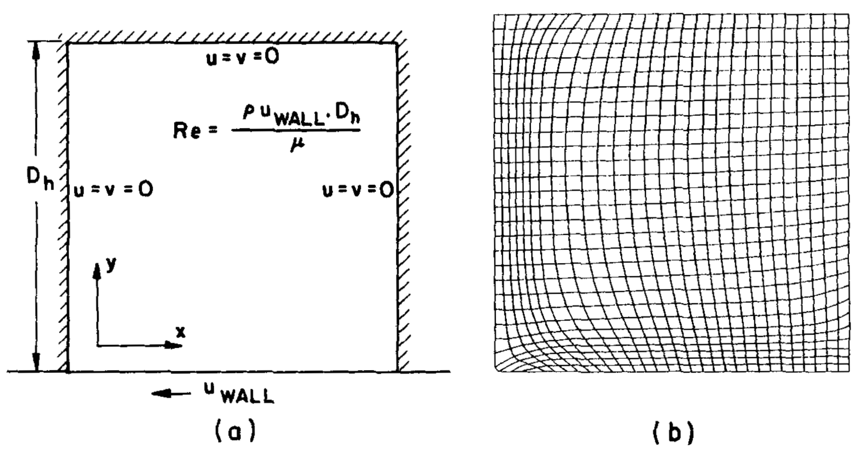

Figure 6. Nomenclature for the sliding lid problem, and the non-orthogonal grid used. The problem was also solved using an orthogonal grid

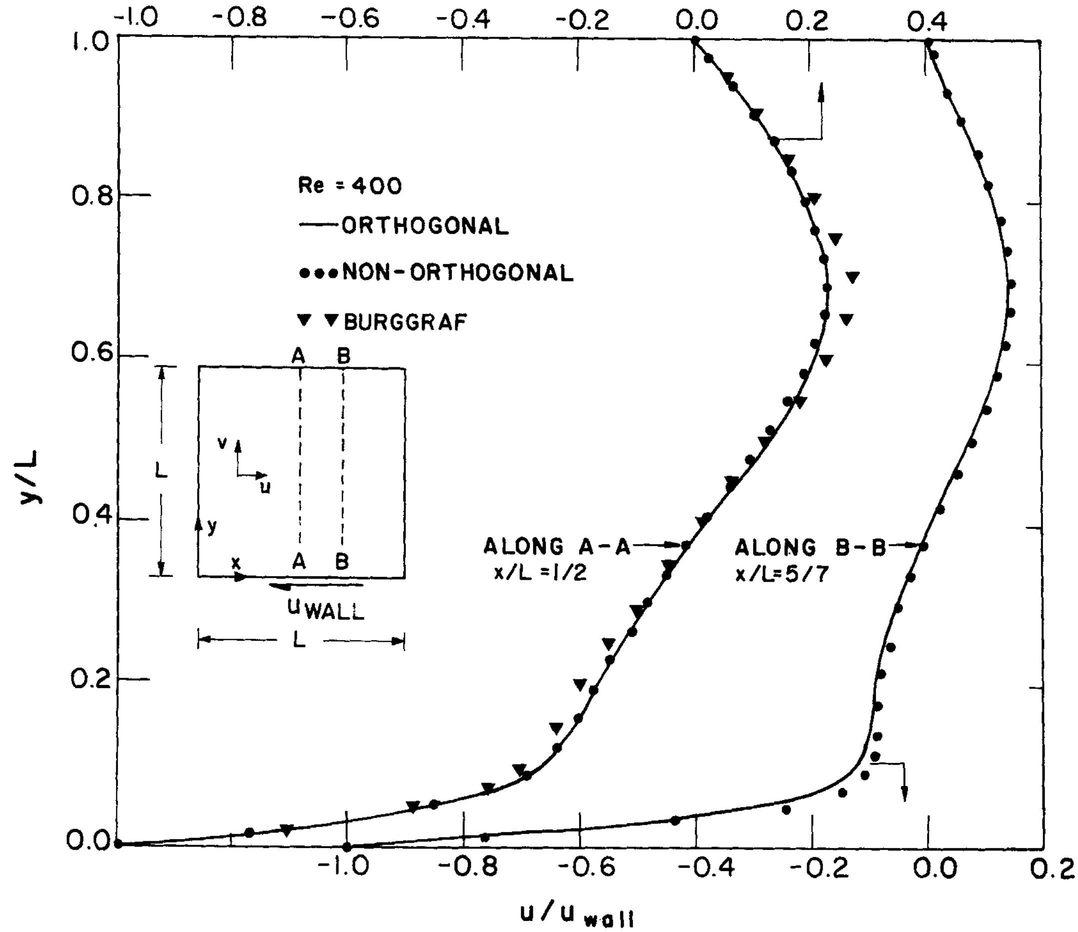

Figure 7. Velocity distributions along 4 lines through the cavity driven by the moving lid

figure also shows that these velocities are in slight disagreement with Burggraf's[27] predictions. The combination of the coarse grid and upstream differences used in the present study are thought to have caused this discrepancy. Similar discrepancies are discussed by Varejao.[28]

The number of coefficient updates to obtain solutions that were converged to the same tolerance was nearly the same for both the Cartesian and non-orthogonal grids. Furthermore, the number of iterations to obtain a specified convergence on the P'-equation was nearly the same for both grids, which suggests that the presence of the corner points in equation (16) (i.e. P'_{NW}, P'_{NE}, P'_{SW}, P'_{SE}) does not strongly affect convergence. The computer time for $Re = 100$ was approximately 8 CPU-minutes on a 370/158 IBM computer. No effort was devoted to optimizing the code to reduce run times for this problem, or for the other solutions described below.

Laminar entrance flow in a circular duct

In order to test the axial flow equation using non-orthogonal grids, the entrance flow in a circular duct was solved. The 15×15 grid that was used is shown as an inset in Figure 8. This

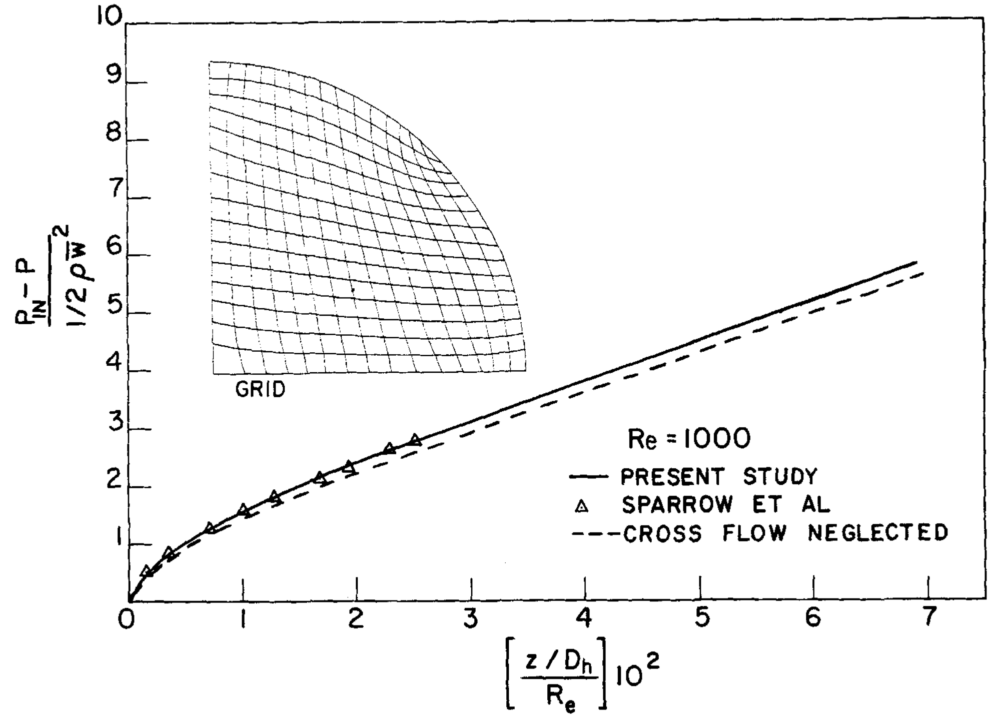

Figure 8. Grid used to compute flow development in a circular duct (insert), and the computed pressure distribution in the axial direction

Figure also shows the predicted dimensionless pressure gradient along the duct axis compared with the results of Sparrow, Lin, and Lundgren,[29] and the results obtained when the cross-flow velocities are set to zero. A small effect of the cross-flow velocities on the axial pressure distribution is, as already pointed out, usually found for the entrance flow in any straight duct of constant cross-section. The predicted development of the centreline velocity was found to be in excellent agreement with the analytical results of Sparrow, Lin, and Lundgren[29] and with the experimental results of Reshotko.[30]

Parabolic flow in ducts with changing cross-sectional areas

Jeffery–Hamel flow. A similarity solution exists[31,32] for two-dimensional flow in a diverging or converging duct with plane walls. The ability of the method and the code to treat ducts with non-parallel walls was tested by solving this problem. A 16×16 Cartesian mesh was placed at several stations in the axial (z) direction so that the grid was non-orthogonal in the x–z and y–z planes. The similarity solution was prescribed at the inlet of a diverging channel and the solution obtained. The predictions at various axial stations were found to be in excellent agreement with the exact solution. Details of these calculations are described by Maliska.[19]

Flow in a converging-diverging duct. With the individual components of the code tested, predictions were made for the duct shown in Figure 9(a). The entrance to the duct is rectangular with an aspect ratio of 3; with increasing z the duct expands in the x-direction and contracts in the y-direction in such a way that it becomes circular at the outlet. Nine

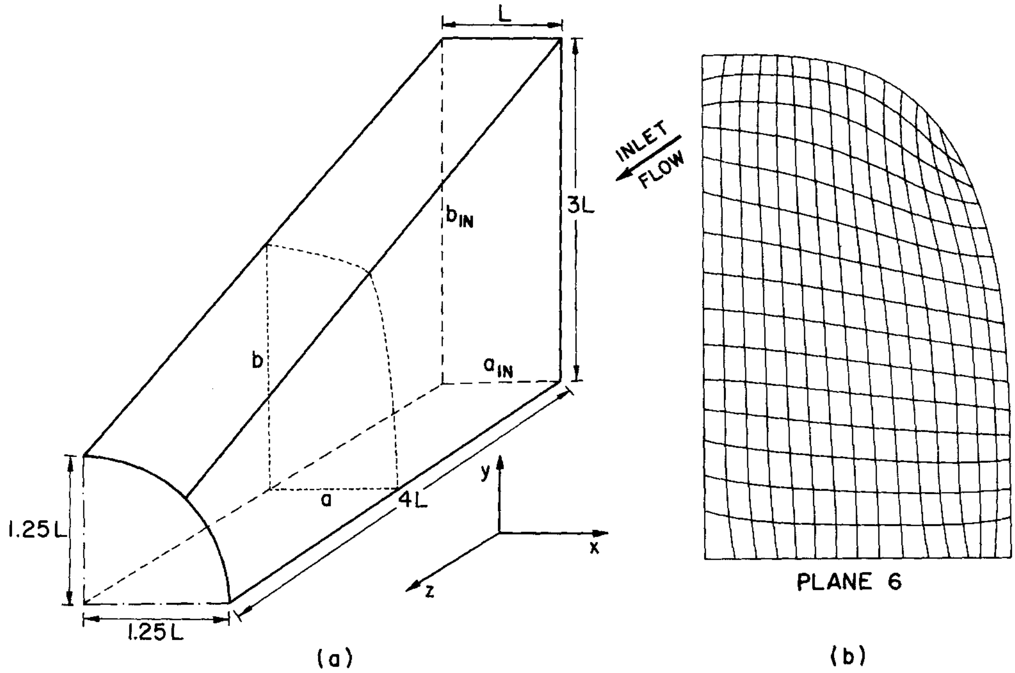

Figure 9. Duct with variation of cross-section with axial distance, and the grid at plane 6

solution planes (including the inlet and outlet) were used with an equal spacing in the z-direction of 1/6th of the inlet hydraulic diameter. The locations of these z-planes are listed in Table II.

The equation which describes the contour of the duct cross-section is:

$$\left(\frac{x}{a}\right)^m + \left(\frac{y}{b}\right)^m = 1$$

where a and b are the half-duct dimensions in the x and y directions (see Figure 9(a)). This expression yields a rectangular duct for $m \to \infty$, and a circular duct if $m = 2$ and $a = b$. The

Table II. Constants defining the boundary shape of the converging-diverging duct. D_H is the hydraulic diameter at the inlet

Plane N	b/a	m	z/D_h
1	3·000	∞	0
2	2·696	18·58	1/6
3	2·411	9·115	2/6
4	2·142	5·957	3/6
5	1·888	4·377	4/6
6	1·648	3·428	5/6
7	1·421	2·794	6/6
8	1·205	2·340	7/6
9	1·000	2	8/6

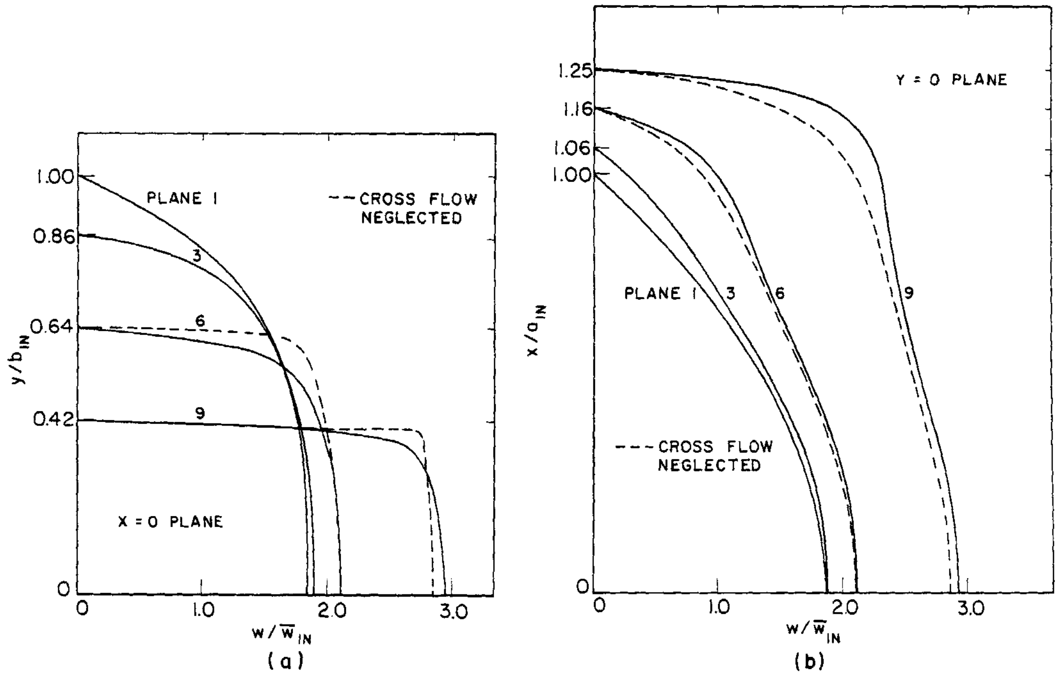

Figure 10. Distributions of axial velocity along the axes of the duct in Figure 9(a)

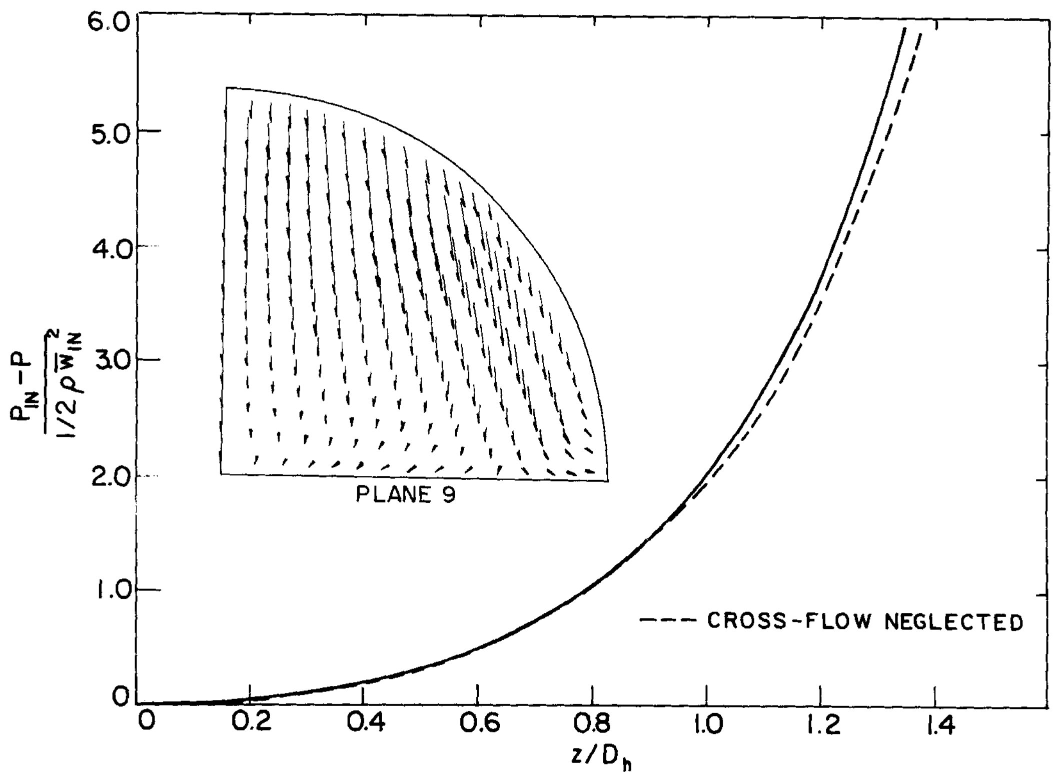

Figure 11. Predicted axial pressure distribution in duct shown in Figure 9(a). The insert shows the velocity vectors on the outlet plane

values of b/a and of m for each calculation plane are listed in Table II. Using this equation for the boundary, a 15×15 grid was generated for each axial plane. The grid on plane 6 is shown in Figure 9(b), and grid at the outlet plane was similar to that in Figure 8. A fully developed velocity profile for a rectangular duct was used as the inlet condition.

Inlet axial velocity profiles on plane 1, and w-velocity predictions on planes 3, 6, and 9 are shown in Figure 10 for the planes $y = 0$ and $x = 0$. The strong contraction of the duct in the y-direction causes the profiles on $x = 0$, Figure 10a, to be flatter. The slight expansion of the boundary in the x-direction results in an inflection in the profile in the plane $y = 0$ in Figure 10(b). The cross-flow velocity vectors on plane 9, shown in the insert in Figure 11, show the strong flow induced by the contraction and the stagnation point on the $y = 0$ plane. The pressure distribution along the duct is also shown in Figure 11.

For ducts with unchanging cross-sections, the axial pressure gradient and axial velocity profiles were found to be very nearly the same for the computed cross-flow as for zero cross-flow velocities. To determine the effect of the cross-flow velocities for this problem u and v were held at zero while the axial velocities and pressure gradient were computed. The resulting axial velocity profiles are indicated as dotted lines in Figure 10 and the corresponding pressure gradient is similarly denoted in Figure 11. Even for such rapid changes in cross-sectional area, the results are little affected. There are, however, no inflection points in the axial velocity profile when the cross-flow is ignored.

The predictions for this problem (15×15 grid at 9 stations) required about 4 CPU-minutes.

DISCUSSIONS AND CONCLUSIONS

The main goal of the research described in this paper was the development of a numerical method for the solution of three dimensional parabolic fluid flow problems in ducts of arbitrarily varying cross-section. Attention was focused on fundamental aspects of the numerical modelling process related to the use of non-orthogonal grids. The numerical results have shown that the use of natural non-orthogonal curvilinear systems for 3D parabolic problems is encouraging, and that an extension to 3D elliptic problems is viable.

Concerning the fundamental aspects analysed, it was seen that the decision to keep the Cartesian components of the velocity vector as dependent variables in the transformed plane, together with the use of the contravariant velocities in the mass conservation balance, gives rise to simple equations and promotes stability for the numerical procedure. It was also demonstrated that the grid layout dictates the number of points involved in the pressure (or P') equation and, what is more important, it is responsible for the type of linkage between the pressure at a point P and its neighbouring pressures. Furthermore, this type of linkage will influence the convergence characteristics of the pressure or pressure-correction (P') equation. Finally, the method reverts to a standard 5-point equation when the grid becomes orthogonal.

The code was fully tested by solving two-dimensional elliptic problems and three-dimensional parabolic problems in ducts with varying cross-section.

ACKNOWLEDGEMENTS

The first author has been supported throughout this study by the Universidade Federal de Santa Catarina and the CNPq (Brazilian Council of Research). Funds for computing were supplied by the Department of Mechanical Engineering, University of Waterloo.

The authors wish to acknowledge many helpful discussions with, and assistance from, J. P. Van Doormaal. This paper is dedicated to the memory of Professor S. A. Alpay, with whom the first author began his Ph.D. studies. Professor Alpay was a gentleman, with a keen mind and unbounded enthusiasm; he is greatly missed by all of us.

NOMENCLATURE

A_E, A_W, etc.	influence coefficients in the finite difference equation for ϕ
B_P^{ϕ}	source term in the finite-difference equation for ϕ
C_1, C_2, C_3, C_4	transformed diffusion coefficients
E	relaxation factor used in the implicit calculations
J	Jacobian of the transformation
P	pressure variation in the duct cross-section
$\bar{P}$	average pressure in the duct cross-section
P'	pressure correction
$\hat{P}^{\phi}$	pressure term in the ϕ momentum equation
P^{ϕ}	transformed pressure term in the momentum equation
P, Q	source terms in the grid generation equations
Re	Reynolds number (defined for each case)
S^{ϕ}	source term in the equation for ϕ
$\hat{S}^{\phi}$	transformed source term in the equation for ϕ
u, v, w	Cartesian velocities
U, V, W	contravariant velocities written without metric normalization
u^*, v^*, w^* / U^*, V^*, W^*	tentative velocity field
x, y, z	Cartesian co-ordinate system
ξ, η, Γ	general curvilinear system, transformed domain
ρ	density
σ_1, σ_2, etc.	boundary of the domain in the physical plane
ϕ	a general scalar field

Subscripts

D	refers to the downstream calculation plane
P, E, N, S, SE / NE, SW, etc.	indicates the location where the variables are evaluated
U	refers to the upstream calculation plane
x, y, z / ξ, η, Γ	partial derivatives of first order

REFERENCES

1. A. M. Winslow, 'Numerical solution of the quasi-linear Poisson equation in a nonuniform triangle mesh', *J. Comp. Physics*, **2,** 149–172 (1967).
2. W. H. Chu, 'Development of a general finite difference approximation for a general domain, part I: machine transformation', *J. Comp. Physics*, **8,** 392–408 (1971).
3. J. F. Thompson, F. C. Thames, and C. W. Mastin, 'Automatic numerical generation of body-fitted curvilinear coordinates system for a field containing any number of arbitrary two dimensional bodies', *J. Comp. Physics*, **15,** 299–319 (1974).

4. A. A. Amsden and C. W. Hirt, 'A simple scheme for generating curvilinear grids', *J. Comp. Physics*, **11,** 23–30 (1973).
5. R. Meyder, 'Solving the conservation equations in fuel rod bundles exposed to parallel flows by means of curvilinear orthogonal coordinates', *J. Comp. Physics*, **17,** 53–67 (1975).
6. S. B. Pope, 'The calculation of turbulent recirculating flows in general orthogonal coordinates', *J. Comm. Physics*, **26,** 197–211 (1978).
7. C. D. Mobley and R. J. Stewart, 'On the numerical generation of boundary fitted orthogonal curvilinear coordinate system', *J. Comp. Physics*, **34,** 124–135 (1980).
8. V. Ramachandra and D. B. Spalding, 'A nonorthogonal finite difference formulation for the three dimensional duct flow' in *Turbulent Forced Convection in Channels and Rod Bundles, Proceedings of NATO Advanced Study Institute*, 1978.
9. N. A. Phillips, 'A coordinate system having some special advantages for numerical forecasting', *J. Meterology*, **14,** 184–185 (1957).
10. J. F. Thompson, F. C. Thames, and C. W. Mastin, 'Boundary fitted curvilinear coordinate system for solution of partial differential equations on fields containing any number of arbitrary two dimensional bodies', *Report CR-2729*, NASA Langley Research Centre, 1976.
11. F. C. Thames, J. F. Thompson, C. W. Mastin, and R. L. Walker, 'Numerical solutions for viscous and potential flow about arbitrary two-dimensional bodies using body-fitting coordinate systems', *J. Compl. Physics*, **24,** 245–273 (1977).
12. J. L. Steger, 'Implicit finite difference simulation of flow about arbitrary two-dimensional geometries', *AIAA J.*, **16,** 679–686 (1978).
13. Z. U. A. Warsi, K. Devarayalu, and J. F. Thompson, 'Numerical solution of the Navier–Stokes equations for arbitrary blunt bodies in supersonic flows', *Numerical Heat Transfer*, **1,** 499–516 (1978).
14. J. K. Hodge, A. L. Stone, and T. E. Miller, 'Numerical solution for airfoils near stall in optimized boundary fitted curvilinear coordinates', *AIAA J.* **17,** 458–464 (1978).
15. T. H. Pullian and J. L. Steger, 'Implicit finite difference simulations of three-dimensional compressible flow', *AIAA J.* **18,** 159–167 (1980).
16. K. N. Ghia, U. Ghia, and C. J. Studerus, 'Analytical formulation of three-diemsional laminar viscous flow through turbine cascade using surface oriented coordinates', *ASME Paper 76-FE-22*, March 1976.
17. D. W. Roberts and C. K. Forester, 'Parabolic procedure for flow in duct with arbitrary cross-section', *AIAA J.* **17,** 33–40 (1979).
18. S. P. Vanka, B. C. J. Chen, and W. T. Sha, 'A semi implicit calculation procedure for flows described in boundary fitted coordinate system', *Numerical Heat Transfer*, **3,** 1–19 (1980).
19. C. R. Maliska, 'A solution method for three-dimensional parabolic fluid flow problems in nonorthogonal coordinates', *Ph.D. Thesis*, University of Waterloo, Canada, 1981.
20. S. V. Patankar and D. B. Spalding, 'A calculation procedure for heat, mass and momentum transfer in three-dimensional parabolic flows', *Int. J. Heat and Mass Transfer*, **15,** 1787–1806 (1972).
21. R. Peyret and H. Viviand, 'Computation of viscous compressible flow based on the Navier–Stokes equation', *AGARD 212*, North Atlantic Treaty Organization, 1975.
22. G. D. Raithby and G. E. Schneider, 'Numerical solution of problems in incompressible fluid flow: treatment of the pressure–velocity coupling', *Numerical Heat Transfer*, **2,** 417–440 (1979).
23. S. V. Patankar, *Numerical Heat Transfer and Fluid Flow*, Hemisphere Publishing Corporation, 1980.
24. F. H. Harlow and J. E. Welch, 'Numerical calculation of time dependent viscous incompressible flow of fluid with free surface', *Physics of Fluids*, **8,** 2182–2189 (1965).
25. G. D. Raithby and K. E. Torrance, 'Upstream-weighted differencing schemes and their application to elliptic problems involving fluid flow', *Computers and Fluids*, **2,** 191–206 (1974).
26. S. V. Patankar, Personal communication, 1979.
27. O. R. Burggraf, 'Analytical and numerical studies of the structure of steady separated flow', *J. Fluid Mechanics*, **24,** 113–151 (1966).
28. L. M. C. Varejao, 'Flux-spline method for heat, mass and momentum transfer', *Ph.D. Thesis*, University of Minnesota, December, 1980.
29. E. M. Sparrow, S. H. Lin, and T. S. Lundgren, 'Flow development in the entrance region, of tubes and ducts', *The Physics of Fluids*, **7,** 338–347 (1964).
30. E. Reshotko, *Report No. 20-364*, Jet Propulsion Laboratory, 1958.
31. F. M. White, *Viscous Fluid Flow*, McGraw-Hill, 1974.
32. K. Millsaps and K. Pohlhausen, 'Thermal distributions in Jeffrey–Hamel flows between nonparallel plane walls', *J. Aeronautical Sci.*, **20,** 187–196 (1953).
33. G. D. Raithby, 'Prediction of dispersion by surface discharge', Basin Investigation and Modelling Section, Canada Centre for Inland Waters, Burlington, Ontario, Canada, 1976.